

1 **A case study of the large-scale traveling ionospheric disturbances in the East**
2 **Asian sector during the 2015 St. Patrick's Day geomagnetic storm**

3
4 Jing Liu¹, Dong-He Zhang^{1*}, Anthea J. Coster², Shun-Rong Zhang², Guan-Yi Ma³, Yong-Qiang
5 Hao¹, Zuo Xiao¹.

6
7 1, Department of Geophysics, Peking University, Beijing, China, 100871

8 2, MIT Haystack Observatory, Westford, Massachusetts, USA

9 3, National Astronomical Observatories, Chinese Academy of Sciences, Beijing, China

10
11
12 **Abstract**

13 This study presents a comprehensive observation of the large-scale traveling ionospheric
14 disturbances (LSTIDs) in the East Asian sector during the 2015 St. Patrick's Day (March 17, 2015)
15 geomagnetic storm. For the first time, 3 dense networks of GPS receivers in China and Japan are
16 combined together to obtain the 2-dimensional (2D) vertical total electron content (VTEC)
17 perturbation maps in a wider longitudinal range than previous works in this region. Results show
18 that a trough of LSTID spanning at least 60° in longitude (80°E-140°E) occurs and propagating
19 from high to lower latitudes around 09:40-11:20 UT. It is followed by a crest of LSTID which
20 shows a tendency of dissipation starting from the East side. The manifestation of the 2D VTEC
21 perturbation maps is in good agreement with the recordings from 2 high-frequency Doppler shift
22 stations and the iso-frequency lines from 8 ionosondes. Then, the propagation parameters of the
23 LSTIDs are estimated by applying least square fitting methods to the distinct structures in the 2D
24 VTEC perturbation plots. In general, the propagation parameters are observably longitudinal
25 dependent. For example, the propagation direction is almost due southward between 105°E-115°E,
26 while it is slightly South by West/East in the West/East side of this region. This feature is probably
27 related to the regional geomagnetic declination. The mean values of the period, trough velocity
28 (V_t), crest velocity (V_c), and wavelength of the wavelike LSTIDs in the studied longitudinal
29 bands are 74.8 ± 1.4 minutes, 578 ± 16 m/s, 617 ± 23 m/s, and 2691 ± 80 km, respectively. Finally,
30 using the VTEC map data from the Madrigal database of the MIT Haystack Observatory, the
31 characteristics of the ionospheric disturbances over the European sector (30°N-70°N, 10°E-20°E)
32 are also studied. The results are very different from those in the East Asian sector in parameters
33 like the occurrence time, oscillation period, and propagation velocities.

34
35
36 **Keywords: Geomagnetic Storm; LSTID; GPS TEC.**
37
38
39

1 1. Introduction

2 During the geomagnetic storm, the solar wind energy is impulsively or continually injected
3 into the earth polar region and making the atmospheric and ionospheric states deviate greatly from
4 their background levels [Fuller-Rowell et al., 1994]. In general, the response of the ionosphere to
5 the geomagnetic storm is classified by a variety of different features, one of which is the large
6 scale traveling ionospheric disturbance (LSTID) that is the wave-like perturbation mainly
7 propagating equatorward from high latitudes. Traveling ionospheric disturbances (TIDs) are
8 classified into LSTIDs and Medium-scale TIDs and they are considered to be the ionospheric
9 manifestation of the presence of atmospheric gravity waves (AGWs) stimulated by different
10 sources. LSTIDs are mainly caused by Joule heating or Lorenz-drag forcing in the Auroral regions
11 during geomagnetic storm period [Hines, 1960; Richmond and Roble, 1979; Hocke and Schlegel,
12 1996].

13 In earlier years, the acquisition of the continuous evolution of LSTIDs on a global scale was
14 limited by the availability of the ionospheric observations. In order to obtain the propagation
15 characteristics of LSTIDs on a large spatial scale, researchers needed to organize their findings
16 from limited ionospheric observations, for example, the foF2 data from sparsely distributed
17 ionosondes. In the 1980s, the GPS method was introduced into the ionospheric study [Klobuchar,
18 1986; Lanyi and Roth, 1988; Coster and Gaposchkin, 1989]. With the dense and worldwide
19 distributed GPS receivers, some characteristic ionospheric phenomena, like traveling ionospheric
20 disturbances (TIDs) [Saito et al., 1998; Tsugawa et al., 2004; Ding et al., 2007], ionospheric
21 storms [Ho et al., 1996], and ionospheric responses to solar flares [Afraimovich, 2000a; Zhang
22 and Xiao, 2005] were revisited frequently and new results were obtained.

23 The propagation characteristics of LSTIDs are always topics of great research interest
24 [Hunsucker, 1982; Ho et al., 1996; Balthazor and Moffett, 1999; Afraimovich et al., 1998, 2000;
25 Shiokawa et al., 2002; Tsugawa et al., 2003, 2004; Ding et al., 2008, 2014; Borries et al., 2009,
26 2017; Habarulema et al., 2015, 2016, 2018; Zakharenkova et al., 2016; Figueiredo et al., 2017;
27 Pederick et al., 2017; Cherniak et al., 2018; Lyons et al., 2019]. Based on limited GPS stations
28 measurements, Afraimovich et al. [1998] propose a radio interferometry method to roughly
29 estimate horizontal propagation velocities and phase front angles of TIDs. Further, the world-wide
30 or local dense distribution of the GPS receivers networks facilitates the acquisition of the global or
31 regional TEC perturbation maps with high spatial and temporal resolutions to reveal the detailed
32 propagating characteristics of TIDs [Ho et al., 1996; Saito et al., 1998; Tsugawa et al., 2004;
33 Borries et al., 2009; Ding et al., 2012]. With more than 60 GPS receivers distributed worldwide,
34 Ho et al. [1996] studied the global distribution of TEC variations and perturbations during a
35 magnetically disturbed period. They identified a TID propagating from the northern sub-auroral
36 region to lower latitudes at a speed of about 460 m/s. The GPS Earth Observation Network
37 (GEONET) in Japan is one of the densest GPS receiver networks on the Earth, and utilizing its
38 data two-dimension (2D) TEC perturbations over Japan can be mapped. With these
39 high-resolution TEC perturbation maps, the spatial structures and temporal evolutions of a TID in
40 the nighttime mid-latitude ionosphere over Japan were revealed clearly [Saito et al., 1998]. Since
41 then, with this dense GPS network, the characteristics of LSTIDs over Japan are carefully studied
42 through case and statistical analysis, and some propagation features of TIDs in this region are
43 revealed [Saito et al., 2001; Shiokawa et al., 2002; Tsugawa et al., 2003, 2004, 2006].

44 For the LSTID with scales of thousands of kilometers, the extensive spatial coverage of

1 ionospheric observations is undoubtedly useful for capturing its propagation features. In recent
2 years, the GPS data from densely distributed GPS stations in China are used to study LSTIDs in
3 this region [Ding et al., 2012, 2013, 2014; Song et al., 2013]. Based on the GPS data from the
4 Crustal Movement Observation Network of China (CMONOC), Ding et al. [2012] obtains
5 temporal continuous 2D imaging of ionospheric disturbances during the geomagnetic storm on
6 May 28, 2011, and find two LSTIDs moving southwestward with the front width of at least 1600
7 km during different storm phases. In addition, through the comparative climatological study of
8 LSTID over North America and China, the different time dependence of LSTID occurrence over
9 two longitudinal sectors were revealed statistically [Ding et al., 2014]. These studies further
10 emphasize the effectiveness of the large coverage, high-resolution ionospheric observations from
11 GPS networks on the detailed investigation of the ionospheric disturbances structures.

12 The propagating direction of the LSTID during the geomagnetic storm has always been
13 focused on for the LSTID studies. From case and statistical studies about LSTID during
14 geomagnetic storm period over East-Asia region conducted independently by Chinese and
15 Japanese scientists in recent years, the dominant propagating direction of LSTID in China and
16 Japan is a little different. It mainly propagates South by West in China region [Ding et al., 2014],
17 while it mainly propagates South by East in Japan region [Tsugawa et al., 2004]. Although the
18 geomagnetic declination is considered to be one of the main factors to be responsible for the
19 propagating direction of LSTID based on different LSTID studies, the LSTID studies concerning
20 the same geomagnetic storm using both China and Japan GPS networks together have not yet been
21 reported.

22 During the period of 17–18, March 2015, the strongest geomagnetic storm in the 24th solar
23 cycle occurred and LSTIDs are detected and analysed in different longitudinal sectors [Ramsingh
24 et al., 2015; Borries et al., 2016; Zakharenkova et al., 2016; Habarulema et al., 2018]. Meanwhile,
25 two high frequency (HF) Doppler stations operated by China Meridional Project [Wang, 2010] at
26 mid-latitude China record large ionospheric HF Doppler shifts after 10:00 UT, which seem to
27 indicate the LSTIDs in the Asian region between 09:00-12:00 UT that reported by Habarulema et
28 al. [2018]. In this study, the multi-network of densely distributed GPS receivers, the HF Doppler
29 stations, and an ionosonde network are used to conduct a more comprehensive study on the
30 propagating characteristics of the disturbances in the East Asian region, especially on the
31 characteristics of the dominant propagating direction over China and Japan.

32 2. Data and Methods

34 Figure 1 illustrates the locations of ground-based receivers that are used in this study from 4
35 Global Navigation Satellite Systems (GNSS) networks distinguished by colors. They are Chinese
36 Meteorological GNSS Network (CMGN), CMONOC in China, GEONET in Japan, and
37 International GNSS Service (IGS). These receivers are selected through data quality checking and
38 regional restriction ($10^{\circ}\text{N} \sim 60^{\circ}\text{N}$, $70^{\circ}\text{E} \sim 150^{\circ}\text{E}$), and the numbers of used stations are 259, 220,
39 1300, and 31 for CMGN, CMONOC, GEONET, and IGS, respectively. The sample rate of all GPS
40 data is 30 seconds. Combining the carrier phase and pseudo-range measurements in two L-band
41 frequencies of GPS receivers' observations, the vertical TEC can be obtained. In the calculation,
42 the height of the ionospheric thin shell is set to be 400 km, and the cutoff elevation angle is 30
43 degrees. The detailed process of the TEC calculation from GPS data can be found in our previous
44 works [Zhang et al., 2009; Zhang et al., 2010].

1 Different methods have been used for extracting the TEC perturbations related to LSTIDs in
 2 previous works [Wan et al., 1997; Afraimovich et al., 2000; Shiokawa et al., 2002; Nicolls et al.,
 3 2004; Tsugawa et al., 2004; Ding et al., 2007]. Afraimovich et al. [2000] suggest that the LSTID
 4 characteristics in TEC can be determined by removing the trend with 3 to 5 order polynomials in
 5 order to eliminate the trends introduced by the motion of satellites and variations of the regular
 6 ionosphere. For a similar purpose, Shiokawa et al. [2002] subtract a running average of TEC over
 7 1 hour from the raw TEC. With more than 1000 GPS receivers over Japan, a series of 2D TEC
 8 perturbation maps can be obtained. Ding et al. [2007] develop another method of obtaining the 2D
 9 TEC perturbation maps by expressing the vertical TEC as a one-order function of local time and
 10 latitude. According to their argument, this method is sufficient to remove background trends for
 11 continuous observation of a GPS receiver-satellite pair without introducing artificial perturbations.
 12 After comparing the results of these methods, a method similar to Ding et al. [2007] is conducted
 13 in this study, in which the vertical TEC at an ionospheric pierce point (IPP) is treated as a function
 14 of universal time (UT), longitude (Lon), and latitude (Lat), i.e.,

$$VTEC_0 = C_0 + C_1UT + C_2Lon + C_3Lat \quad (1)$$

$$VTECP = VTEC - VTEC_0 \quad (2)$$

15 in which $VTEC_0$ is the background change and $VTECP$ is VTEC perturbation. Then, the obtained
 16 $VTECP$ data is reorganized into pixels which are bounded by 10°N ~ 60°N, 70°E ~ 150°E and
 17 with a spatiotemporal resolution of 1°longitude × 1°latitude × 10 minutes. The $VTECP$ value for
 18 each pixel is set to be the average of all $VTECP$ data of which the IPP and UT locate in this pixel.
 19 After these steps, the featured ionospheric disturbances are expected to appear on a series of 2D
 20 $VTECP$ maps.

21 As a comparison, the VTEC map from Madrigal database of the MIT Haystack Observatory
 22 (<http://cedar.openmadrigal.org/>) is used to reveal the ionospheric disturbances in the European
 23 sector (30°N ~ 70°N, 10°E ~ 20°E). This database provides worldwide VTEC values in 1°latitude
 24 × 1°longitude pixels with a temporal resolution of 5 minutes [Rideout and Coster, 2006] and has
 25 good data coverage in European and American sectors. VTEC maps with such a high
 26 spatiotemporal resolution are suitable to reveal the structures of traveling ionospheric disturbances
 27 [Zhang et al., 2017].

28 The Doppler shift data observed at two high frequency (HF) Doppler sounding stations in
 29 China is collected, of which the station codes are MDT (40.4°N, 116.9°E), and SZT (22.6°N,
 30 114.1°E). The sounding system continuously receives electromagnetic waves with a stabilized
 31 frequency of 10 MHz transmitted by the National Time Service Center (NTSC) (35.7°N, 109.6°E)
 32 to detect the ionospheric disturbances through the Doppler shifts of this standard frequency. These
 33 shifts are considered to be caused by ionospheric variations mainly around the reflecting point of
 34 the electromagnetic wave in the ionosphere. According to the geometrical relationships, the
 35 locations of the reflecting point for MDT and SZT are (38.0°N, 113.2°E) and (29.2°N, 111.8°E),
 36 respectively. These stations are marked in Figure 1 with colored stars.

37 In this study, ionograms from 8 ionosonde stations in China middle latitude are used to derive
 38 the iso-frequency lines, which vary as a function of universal time and virtual height. The sample
 39 rate of the ionograms is 15 minutes. These ionosondes belong to the China Research Institute of
 40 Radio-wave Propagation (CRIRP) and their locations are marked in Figure 1 with green triangles.
 41 The virtual height data is manually scaled by ourselves to reduce possible errors of auto scaling
 42 [Krankowski et al., 2011; Habarulema and Carelse, 2016] from these ionograms with professional

1 scaling software provided by CRIRP. During the scaling, we limited the frequency to be less than
2 7 MHz. In addition, the condition of the geomagnetic storm is shown with data from the high
3 resolution (5 minutes) OMNI dataset, which is downloaded from the FTP service of the NASA
4 Goddard Space Flight Center (<https://spdf.gsfc.nasa.gov>).

6 3. Results

7 3.1 Observations

8 Figure 2 shows the variations of (a) solar wind speed, (b) interplanetary magnetic field (IMF)
9 B_z component, (c) the SYM-H index, and (d) the AE index from the OMNI dataset, and the time
10 range is from 18:00 UT, 16 March 2015 to 06:00 UT, 18 March 2015. It should be noted that the
11 solar wind magnetic field and plasma data are time-shifted to the bow shock nose to better support
12 the solar wind-magnetosphere coupling studies. It can be seen clearly that a geomagnetic storm
13 occurred on 17 March 2015, with the sudden storm commencement (SSC) at $\sim 04:45$ UT, which is
14 characterized by a sharp increase (marked with vertical dashed lines) in the solar wind speed, B_z ,
15 and SYM-H index. The main phase of the storm can be roughly divided into two stages. The first
16 stage is from $\sim 06:00$ UT, when the IMF B_z component first turns to southward, to $\sim 12:00$ UT,
17 when the B_z turns southward again after back to northward for about 2 hours. After $\sim 12:00$ UT,
18 the B_z is southward for the most time, until it enters the recovery phase. The SYM-H and AE
19 indices show a similar two-stage feature as the B_z . The SYM-H decreases after $\sim 06:00$ UT,
20 reaches the first minimum at $\sim 09:30$ UT, and increases to a local maximum at $\sim 12:00$ UT. Then,
21 it gradually decreases with small oscillations and reaches the minimum value of -233 nT at \sim
22 $22:45$ UT. Correspondingly, the AE index exhibits the first increase period between 06:00 UT to
23 12:00 UT, with the maximum intensity of ~ 1000 nT, and the second period between 12:00 UT to
24 02:00 UT of the next day, during which the AE increases much larger with several peaks. This
25 storm is the strongest one in the 24th solar cycle [Astafyeva et al., 2015].

26 During the first stage of the main phase, disturbances are observed successively at MDT and
27 SZT Doppler receiver stations. Figure 3 illustrates the variations of the Doppler shift records at (a)
28 MDT and (b) SZT between 08:00 UT and 14:00 UT on 17 March 2015. It shows that two distinct
29 positive shifts occur at about 10:22 UT and 10:53 UT, respectively. Shortly after, it exhibits two
30 negative shifts but with much smaller amplitudes. Suppose these successive disturbances indicate
31 a propagating perturbation, according to the estimated locations of the reflecting points that
32 mention above and the occurrence time of the two positive peaks, the approximate speed of this
33 perturbation is about 535 m/s. This value is much larger than the speed of the movement of the
34 ionospheric negative storm that usually occurs in the middle latitude due to storm-induced
35 equatorward wind [Buonsanto, 1999], and the ionospheric storm is not serious in the Asian sector
36 during this period [Astafyeva et al., 2015]. Considering the magnitude of the speed and the time
37 interval of the positive-negative variations, the recorded perturbations probably reflect an
38 equatorward propagating LSTID in the East Asian sector.

39 To confirm this, Figure 4 presents a sequence of 2D VTECP maps between 09:40-11:40 UT
40 on 17 March 2015 with the method described in section 2. The grey areas represent the night side.
41 Note that the raw value of VTECP is converted into $VTECP'$ with the equation

$$VTECP' = \text{sgn}(VTECP) * \log_{10}(\text{abs}(VTECP) + 1) \quad (3)$$

42 This transform provides a better colormap for 2D VTECP plots by sharpening the edges between
43 positive and negative values and reduce the differences of VTECP in middle and low latitudes.

1 The yellow lines illustrate the least square fitting results for all the negative pixels within certain
2 rectangular areas bounded by longitudes and latitudes. The green lines are similar but for pixels
3 with the bottom 5% absolute VTECP' values in selected areas (see section 3.2 for a detailed
4 example). These two kinds of lines mark the approximate locations of the wavefronts.

5 A large-scale wavelike perturbation can be seen clearly in Figure 4. The first relatively
6 distinct wave structure emerges during the (d) 10:10-10:20 UT period, while its sign can already
7 be observed as early as (a) 09:40-09:50 UT in the northwest part of China. During (e) 10:20-10:30
8 UT, a negative band that across both China and Japan sectors occur between around 30°N-45°N,
9 which gradually propagates to lower latitudes in the next tens of minutes. During (f) 10:30-10:40
10 UT, the first clear wavefront of the positive band appears, which also shows an equatorward
11 movement for at least half an hour. Finally, there seems to be no distinct wave structure following
12 the positive band. Considering the spatiotemporal characteristics of this perturbation, it can be
13 preliminarily identified as an LSTID. By the way, it is interesting to note that the positive bands
14 do not extend to the Japan sector in (h) and (i), and the corresponding VTECP' amplitudes seem
15 smaller in the East side than in the West side. This may be probably related to that the Japan sector
16 has already entered the nightside.

17 Both the negative and positive bands exhibit more complex variations when they enter the
18 equatorial ionospheric anomaly (EIA) region between 20°N-30°N. On the one hand, the amplitude
19 of VTECP' is relatively larger than those in the higher latitudes. On the other hand, it seems that
20 the equatorward propagating of the negative band decelerates significantly in this area, which is
21 especially shown in (g-l). Such complex features are probably related to the various physical
22 processes in this region. Ding et al. [2012] suggest that LSTIDs experience severe dissipation in
23 South China region due to viscosity and heat conductivity at low latitudes, which may account for
24 the weakening of the equatorward propagating of the wavelike structures. Besides, Pradipta et al.
25 [2016] studied the interaction of the auroral LSTIDs from opposite hemispheres near the dip
26 equator during the 26 September 2011 geomagnetic storm. It shows that such interaction may
27 bring much complexity to the TEC perturbations near the dip equator.

28 Our observations of the Doppler shift and VTECP' maps are in good agreement. To show it
29 clearly, Figure 5 shows the variations of the mean VTECP' data near the Doppler reflection points
30 with the same time range of Figure 3. It can be seen that the troughs at around 10:20 UT in (a) and
31 10:50 UT in (b) correspond well to the two distinct crests in Figure 3. In addition, the variations of
32 the VTECP' between 11:00 and 14:00 are also in a good negative correlation with the Doppler
33 shift observations for each reflecting point. It should be noted that the variation of VTECP' at the
34 reflecting point 1 exhibits more variability than that at the reflecting point 0, especially around
35 09:00 UT, 10:00 UT, and 12:00 UT. Considering that point 1 (29.2°N, 111.8°E) is approaching the
36 EIA region, the causes for VTEC perturbations are more complicated as mentioned above. This
37 feature is consistent with the observations of the 2D VTECP' maps in Figure 4.

38 Ionospheric parameters from ionograms have been commonly used since early TID studies.
39 Recently, ionograms and iso-frequency lines with different sampling rates were used in TID
40 studies [Klausner et al., 2009; Ding et al., 2012, 2013; Pradipta et al., 2015; Ramsingh et al., 2015;
41 Habarulema et al., 2018]. Figure 6 presents the temporal variations of the virtual height for each
42 iso-frequency line. The names and locations of the corresponding ionosondes are given in each
43 subplot as annotates. The sampling frequency are marked on the right side for each line. On the
44 left column, the results of five stations are arranged in order from high to lower latitudes, and on

1 the right column, it shows the recordings of four stations in the same latitudinal belt.. We can see
2 clearly that a distinct uplift of the virtual height occurs at 09:45 UT at Manzhouli station, and it
3 gradually moves equatorward from high to lower latitudes (a-e). Meanwhile, the phase difference
4 is not observed for the stations on the right column. This means that the ionospheric disturbance
5 roughly moves along the meridian line in this longitudinal sector (around 115 E), which
6 corresponds to the results of the 2D VTECP' map. Moreover, although the time resolution of 15
7 minutes is relatively low, it can still be identified that the crests in the higher iso-frequency lines
8 appear earlier than those in the lower ones. Such trends (marked with black dashed lines) indicate
9 a downward vertical phase velocity, which is one of the typical characteristics of TID and AGW
10 [Hine, 1960; Hocke and Schlegel, 1996]. It should be noted that the downward trend is not much
11 clear for certain station, especially the one in Qingdao. This may be attributed to the 15 minutes
12 sampling interval.

13 14 3.2 Estimating Propagation Parameters

15 As preparation for estimating the propagating parameters of this LSTID, Figure 7 shows a
16 detailed example of the wavefront fitting method with the VTECP' map in Figure 4(g)
17 (10:40-10:50 UT). The reason for choosing this period is that the structure of the wavefront is
18 relatively clear, and the boundary of the positive and negative wave band in the Japan sector can
19 still be partly identified. The green line is the least square fitting for the green dots, of which the
20 absolute VTECP' values are close to zero (bottom 5%) among all the dots in a certain region
21 (75 E -140 E , 30 N -40 N). The wave propagating azimuth (marked with arrows) can be estimated
22 with the normal direction of this fitting line. Results are listed in Table 1 in the second column.

23 It can be seen clearly that the TID moves due South around 110 E , and in the West/East
24 region, the propagation direction is slightly South by West/East. It should be noted that the
25 morphology of this TID is continuously changing as it moves from high to lower latitudes in the
26 studied region. Although the azimuths are estimated only with the wavefront data during
27 10:40-10:50 UT, such longitudinal dependence of azimuths corresponds well with other fitting
28 lines in Figure 4(e, f, g, h).

29 In order to derive the phase speed, period, and wavelength of this LSTID, the time-latitude
30 plots (TLPs) of VTECP' are obtained for six longitudinal bands, which are marked with dashed
31 rectangles A-F in Figure 7. For each band, the VTECP' data is averaged along the latitude for
32 every 6 minutes (0.1 hours), and the results as a function of UT and latitude are illustrated
33 correspondingly in Figure 8(a-f). As mentioned before, the variation of VTECP' in the EIA region
34 is rather complex, so only the values over 30 N (marked with dashed lines) are used to estimate
35 the speed.

36 As expected, the most distinctive structures in all panels are the pair of negative and positive
37 bands around 10:40 UT, which correspond to the perturbations moving from high to lower
38 latitudes shown in Figure 4. The structures in the 130 E -140 E are not quite clear, which may be
39 due to the lack of data in some parts of this area, but the trough around 10:40 UT can still be
40 identified. To estimate the meridional phase speeds of these perturbation patterns, the linear least
41 square method is used to fit the pairs of troughs and crests. The data points for the linear fitting are
42 marked with white dots, which are the minimum/maximum values along with each latitudinal bin
43 around the negative/positive structures that we focus on. The phase speeds for wave troughs (V_t)
44 and crests (V_c) can be derived based on the slopes of the fitting lines. Moreover, the period of the

1 wave can be estimated through the time interval between the trough and crest in TLPs. In practice,
2 for each longitudinal region, the average of time lags along all latitudinal bins is set to be the half
3 period of the wave in this region. Finally, with the period and speed, the wavelength can be easily
4 determined.

5 However, those speed, period, and wavelength are the projections on longitudes. After
6 adjusted by the propagation azimuths that calculated above, the final results of the estimated
7 parameters are also listed in Table 1. The longitudinal dependence of these parameters can be seen
8 clearly. The mean values and standard deviations of the period, V_t , V_c , and wavelength are $74.8 \pm$
9 1.4 minutes, 578 ± 16 m/s, 617 ± 23 m/s, and 2691 ± 80 km, respectively. These parameters are
10 typical for an LSTID. Besides, it is interesting to note that the mean V_c is slightly larger than the
11 mean V_t , which seems like the wave behind is pushing that ahead.

12 It is interesting to note that V_t is in reasonable agreement with the result of 535 m/s derived
13 from the Doppler recordings. To show it more specifically, we estimated the speed and direction of
14 the LSTID using the same TLP method as Figure 8 but in 111°E - 114°E and 29°N - 38°N
15 (corresponding to the reflecting points). The result is 562 ± 59 m/s and 0° , respectively. In general,
16 the LSTID velocity estimated from ground-based stations tend to be larger than the actual velocity
17 since these stations, in most cases, are not in perfect alignment with the propagation direction of
18 the LSTID [Afraimovich et al., 1998; Habarulema et al., 2013]. Such good agreement between
19 VTECP' and HF Doppler results may be attributed to the fact that the reflecting points
20 ($29.2^\circ\text{N}, 111.8^\circ\text{E}$; $38.0^\circ\text{N}, 113.2^\circ\text{E}$) of the Doppler receivers are in a narrow longitudinal band and
21 the direction of the LSTID's propagation is also almost due south between 111°E - 114°E .

22 As mentioned above, the VTECP' in the EIA region seems to exhibit different features
23 compared to that in the middle latitude. It can be seen from Figure 8(c) that VTECP' in this region
24 also shows a periodic variation, but its period seems larger and time duration is longer than the
25 LSTID. These disturbances are probably related to the complex variations of VTEC after 08:00
26 UT (around dusk). Besides, the perturbations at 20°N around 12:00 UT and 13:00 UT show
27 patterns of poleward movement. Habarulema et al. [2018] have identified TIDs in the
28 Asian-Australian sector during the same storm period. It provides clear examples of TIDs crossing
29 the dip equator from the southern hemisphere to the northern hemisphere around 09:00-12:00 UT.
30 Their analysis shows that these TIDs may not have exceeded 30°N . Such poleward feature is also
31 detected in other longitudinal sectors during this storm [Zakharenkova et al., 2016] and other
32 storms [Pradipta et al., 2016; Jonah et al., 2018]. In addition, Ding et al. [2013] have studied the
33 poleward-propagating LSTIDs in southern China during a medium-scale storm in 2011. They
34 attribute their observations to the excitation of secondary LSTIDs during the dissipation of
35 primary disturbances from the lower atmosphere. Besides, the poleward-moving disturbances may
36 also be induced by the variation of the equatorial electrojet as pointed out by Chimonas [1970] and
37 more recently by Habarulema et al. [2016]. A detailed investigation of this phenomenon is not
38 the focus of this work.

39 40 **4. Discussion**

41 Our results show that the propagation parameters of the LSTID in the East Asian sector during
42 the St. Patrick's Day storm are longitudinal dependent. Among these parameters, the longitudinal
43 dependence of the propagation azimuth of an LSTID receives much attention in previous works.
44 In general, earlier studies suggest that there are four main factors that affect the direction of a

1 polar originated LSTID, which are the velocity of the background neutral wind [Hines, 1960;
2 Morton and Essex, 1978; Maeda and Handa, 1980], the structure and evolution of the source
3 region in the auroral oval [Maeda and Handa, 1980; Hunsucker, 1982; Ding et al., 2007], the
4 Coriolis force [Maeda and Handa, 1980; Balthazor and Moffett, 1999; Afraimovich et al., 2000;
5 Tsugawa et al., 2004; Ding et al., 2013], and the declination of geomagnetic field [Tsugawa et al.,
6 2004; Borries et al., 2009].

7 The Coriolis force effect is generally believed to contribute to the clockwise shift of the
8 propagation direction of the LSTIDs [Afraimovich et al., 2000; Tsugawa et al., 2004; Ding et al.,
9 2013]. The observations of the shift (10° - 20° on average) are consistent with the calculation by
10 Maeda and Handa [1980] and the model simulation by Balthazor and Moffett [1999]. However, in
11 our study, the shift of the propagation direction is not systematic westward, which means the
12 variability of the LSTID azimuth in our observation cannot be attributed to the Coriolis force, at
13 least not to it alone.

14 The structure/movement of the source region for the LSTID in the auroral oval is another
15 candidate for explaining the longitudinal dependence of the propagation direction of the LSTID.
16 Previous studies have suggested that the westward movement of enhanced electrojets in the
17 auroral arc is an important cause of the westward shift of the LSTID propagation direction at high
18 latitudes [Hunsucker, 1982; Ding et al., 2007]. The change of the propagation direction of LSTIDs
19 as they move from high to middle latitudes during the superstorm of 29 October 2003 over North
20 America, was explained by Ding et al. [2007] as related to a change in the position of the
21 electrojet enhancement area near the auroral oval. Nevertheless, since the structure and the
22 evolution process of the source region during storm period is complicated, more cases and
23 modeling studies are needed to find a clear connection between it and the propagation direction of
24 LSTIDs.

25 In general, the velocity of the neutral wind is much less than that of the LSTIDs, and the
26 thermospheric wind velocity in the same latitudinal belt with a limited longitudinal extension
27 should exhibit little variance. So the contribution of the background wind on the change of the
28 propagating direction would be limited in the absence of the geomagnetic field. However, a
29 combined effect of magnetic declination and zonal wind can cause F region electron density
30 differences between two sides of the zero declination [Zhang et al., 2011]. During storm periods,
31 the enhanced zonal winds [Fuller-Rowell et al., 1994] can intensify these differences [Thomas et
32 al, 2016]. As a result, the geomagnetic declination is considered to be an important factor that
33 affects the propagation direction of the LSTID. Some researchers have studied the predominant
34 propagation direction of LSTIDs during storm periods in different longitudinal sectors, and
35 suggest that, statistically speaking, the predominant directions of LSTID in European continent,
36 China and Japan are primarily southward, South to West and South to East, respectively [Nicolls
37 et al, 2004; Tsugawa et al, 2004; Borries 2009; Ding et al, 2013]. These results are all consistent
38 with the corresponding geomagnetic declination in each sector.

39 In the longitudinal region of 70° E- 150° E, the geomagnetic declination angles change from
40 North by East in the West side to North by West in the East side. This characteristic seems to show
41 some kind of consistent with the azimuth results in Table 1. To illustrate such connection
42 quantitatively, Figure 9 depicts the (a) the geomagnetic declination on the wavefront in different
43 longitudes in Figure 7 and (b) the propagation direction (azimuth- 180°) of the LSTID at the same
44 spot. The connection between these two parameters is quite obvious in this event. This result

1 manifests that the propagation of LSTIDs in different longitudes is probably influenced by the
2 orientation of the geomagnetic field lines in the East Asian sector. In addition, the tendency of
3 field-aligned propagation of the LSTID indicates that it is driven by the neutral winds rather than
4 by electric fields since the winds push the plasma up and down along the magnetic field lines. It
5 should be noted that our speculation needs to be verified with more observational data and
6 numerical simulation to reduce uncertainty in our propagation estimation and to figure out the
7 detailed physical processes.

8 During the 2015 St. Patrick's Day storm, LSTIDs in the European-African, American and
9 Asian-Australian sectors are detected and analysed with TEC observations [Borries et al., 2016;
10 Zakharenkova et al., 2016; Habarulema et al., 2018]. It shows clearly in their results that the
11 European sector also exhibits LSTIDs around 11:00 UT. As a comparison, we also analysed these
12 LSTIDs but with VTEC data from the Madrigal database of the MIT Haystack Observatory. This
13 database has good spatiotemporal coverage for the European and American sectors. To derive the
14 VTECP, a narrow longitudinal band (10°E-20°E, 30°N-70°N) is first selected and the VTEC data
15 with the same latitude at the same time is average. At each latitude bin, the averaged VTEC forms
16 a time series and the temporal resolution is reset to 12 minutes (0.2 hours) with bin averaging.
17 Then, a running mean with a 1.5 hours window is conducted for each time series and their
18 difference is taken as the VTECP. The result is plotted in Figure 10 as a TLP. The fitting lines are
19 obtained with the same method as those in Figure 8.

20 Figure 10 is basically consistent with previous results, such as the synchronous perturbations
21 around 04:45 UT and 09:15 UT, and the LSTID structures between 10:00 UT and 17:00 UT.
22 Moreover, our result shows that the VTECP' behavior between 60°N and 70°N is quite different
23 from below. The pattern around 10:00 UT seems to represent a TID with smaller phase speed.
24 Considering the physical processes are more complex in such high latitudes [Foster et al., 2014],
25 we only focus on the perturbations below 60°N. The phase speeds estimated from the crest and
26 trough are $\sim 500 \pm 51$ m/s and $\sim 427 \pm 55$ m/s, respectively, and the estimated period is $\sim 4.0 \pm 0.2$
27 hours. It is clear that the appearances of the LSTIDs are different in the European and the East
28 Asian sectors during the same UT period for the same storm event. This may be related to the
29 location or structure of the Joule heating source in the auroral oval or the difference of the
30 background TEC in the two sectors. For better understanding this difference, more studies on the
31 Joule heating source are needed.

32 33 5. Summary

34 Using data from 4 GPS receiver networks (CMGN, CMONOC, GEONET, IGS), together
35 with recordings of 2 HF Doppler shift stations and 8 ionosondes, we provide comprehensive and
36 detailed observation results of the LSTIDs in the East Asian sector during the 2015 St. Patrick's
37 Day storm. The GPS receiver networks in China and Japan are combined together to produce 2D
38 VTEC perturbation maps in order to give a wider image of the LSTID structures in the East Asia.
39 As a comparison, the ionospheric disturbances in the European sector are also studied with VTEC
40 data from the Madrigal database. The propagation parameters of the LSTIDs are estimated. Main
41 results can be summarized as follows:

42 (1) A trough of LSTID occurs and propagates from high to lower latitudes during 09:40-11:20
43 UT, which spans over 60° in longitude. It is followed by a crest of LSTID that characterized by a
44 clear tendency to dissipate starting from the East side. These features are in good agreement with

1 observations by HF Doppler shift stations and ionosondes

2 (2) The propagation orientation is almost due southward around 105°E-115°E, and it tends to
3 slightly shift westward/eastward in the West/East part of the studied area. This may be influenced
4 by the regional declination of the geomagnetic field lines.

5 (3) Other propagation parameters are also longitudinal dependent (see Table 1), and the mean
6 values and standard deviations of the period, V_t , V_c , and wavelength are 74.8 ± 1.4 minutes, 578
7 ± 16 m/s, 617 ± 23 m/s, and 2691 ± 80 km, respectively.

8

9 **Acknowledgement:**

10 We are grateful to the International GPS Services (IGS) (<ftp://cddis.gsfc.nasa.gov>). The GPS data
11 from CMONOC and CMGN networks are provided by the China Earthquake Administration
12 (CEA) and the China Meteorological Administration (CMA), respectively. The GPS data from
13 GEONET are provided by the Geographical Survey Institute, Japan. GPS TEC data products and
14 access through the Madrigal distributed data system are provided to the community by the
15 Massachusetts Institute of Technology under support from the US National Science Foundation
16 grant AGS-1242204. The HF Doppler records are from the Chinese Meridian Project. The
17 ionosonde data are provided by the China Research Institute of Radio wave Propagation (CRIRP).
18 We thank the NASA/GSFC's Space Physics Data Facility's OMNIWeb service for data of the
19 interplanetary and SYM-H parameters. This research was supported by the National Natural
20 Science Foundation of China (No. 41674157).

21

22

23 **References**

24 Afraimovich, E. L., Palamartchouk, K. S., and Perevalova, N. P.: GPS radio interferometry of
25 travelling ionospheric disturbances. *Journal of Atmospheric and Solar-Terrestrial*
26 *Physics*, 60(12), 1205-1223, 1998.

27 Afraimovich, E. L., Kosogorov, E. A., Leonovich, L. A., Palamartchouk, K. S., Perevalova, N. P.,
28 and Pirog, O. M.: Determining parameters of large-scale traveling ionospheric disturbances
29 of auroral origin using GPS-arrays. *Journal of Atmospheric and Solar-Terrestrial*
30 *Physics*, 62(7), 553-565, 2000.

31 Astafyeva, E., Zakharenkova, I., and Förster, M.: Ionospheric response to the 2015 St. Patrick's
32 Day storm: A global multi-instrumental overview. *Journal of Geophysical Research: Space*
33 *Physics*, 120(10), 9023-9037, 2015.

34 Balthazor, R. L. and Moffett, R. J.: Morphology of large-scale traveling atmospheric disturbances
35 in the polar thermosphere. *Journal of Geophysical Research: Space Physics*, 104(A1),
36 15-24. Borries, C., Jakowski, N., & Wilken, V. (2009). Storm induced large scale TIDs
37 observed in GPS derived TEC. *Ann. Geophys*, 27(4), 1605-1612, 1999.

38 Borries, C., Mahrous, A. M., Ellahouy, N. M., and Badeke, R.: Multiple ionospheric
39 perturbations during the Saint Patrick's Day storm 2015 in the European - African sector.
40 *Journal of Geophysical Research: Space Physics*, 121(11), 11-333, 2016.

41 Borries, C., Jakowski, N., Kauristie, K., Amm, O., Mielich, J., and Kouba, D.: On the dynamics of
42 large-scale traveling ionospheric disturbances over Europe on 20 November 2003. *Journal of*
43 *Geophysical Research: Space Physics*, 122(1), 1199-1211, 2017.

44 Buonsanto, M. J.: Ionospheric storms—A review. *Space Science Reviews*, 88(3-4), 563-601,

1 1999.

2 Cherniak, I. and Zakharenkova, I.: Large-Scale Traveling Ionospheric Disturbances Origin and
3 Propagation: Case Study of the December 2015 Geomagnetic Storm. *Space Weather*, 16(9),
4 1377-1395, 2018.

5 Chimonas, G.: The equatorial electrojet as a source of long period travelling ionospheric
6 disturbances. *Planetary and Space Science*, 18(4), 583-589, 1970.

7 Coster, A. J. and Gaposchkin, E. M.: Use of GPS pseudo-range and phase data for measurement of
8 ionospheric and tropospheric refraction. In Institute of Navigation Satellite Division, 2nd
9 International Technical Meeting (pp. 439-443), 1989.

10 Ding, F., Wan, W., Ning, B., and Wang, M.: Large-scale traveling ionospheric disturbances
11 observed by GPS total electron content during the magnetic storm of 29-30 October
12 2003. *Journal of Geophysical Research: Space Physics*, 112(A6), 2007.

13 Ding, F., Wan, W., Liu, L., Afraimovich, E. L., Voeykov, S. V., and Perevalova, N. P.: A statistical
14 study of large-scale traveling ionospheric disturbances observed by GPS TEC during major
15 magnetic storms over the years 2003–2005. *Journal of Geophysical Research: Space
16 Physics*, 113(A3), 2008.

17 Ding, F., Wan, W., Ning, B., Zhao, B., Li, Q., Zhang, R., Xiong, B., and Song, Q.:
18 Two-dimensional imaging of large-scale traveling ionospheric disturbances over China based
19 on GPS data. *Journal of Geophysical Research: Space Physics*, 117(A8), 2012.

20 Ding, F., Wan, W., Ning, B., Zhao, B., Li, Q., Wang, Y., Hu, L., Zhang, R., and Xiong, B.:
21 Observations of poleward-propagating large-scale traveling ionospheric disturbances in
22 southern China. In *Annales Geophysicae* (Vol. 31, No. 2, p. 377). Copernicus GmbH, 2013.

23 Ding, F., Wan, W., Li, Q., Zhang, R., Song, Q., Ning, B., Liu, L., Zhao, B., and Xiong, B.:
24 Comparative climatological study of large-scale traveling ionospheric disturbances over
25 North America and China in 2011–2012. *Journal of Geophysical Research: Space
26 Physics*, 119(1), 519-529, 2014.

27 Figueiredo, C. A. O. B., Wrasse, C. M., Takahashi, H., Otsuka, Y., Shiokawa, K., and Barros, D.:
28 Large-scale traveling ionospheric disturbances observed by GPS dTEC maps over North and
29 South America on Saint Patrick's Day storm in 2015. *Journal of Geophysical Research: Space
30 Physics*, 122(4), 4755-4763, 2017.

31 Foster, J. C., Erickson, P. J., Coster, A. J., Thaller, S., Tao, J., Wygant, J. R., and Bonnell, J. W.:
32 Storm time observations of plasmasphere erosion flux in the magnetosphere and
33 ionosphere. *Geophysical Research Letters*, 41(3), 762-768, 2014.

34 Fuller-Rowell, T. J., Codrescu, M. V., Moffett, R. J., and Quegan, S.: Response of the
35 thermosphere and ionosphere to geomagnetic storms. *Journal of Geophysical Research:
36 Space Physics*, 99(A3), 3893-3914, 1994.

37 Habarulema, J. B., Katamzi, Z. T., and McKinnell L.-A.: Estimating the propagation
38 characteristics of largescale traveling ionospheric disturbances using ground-based and
39 satellite data, *J. Geophys. Res. Space Physics*, 118, 7768–7782, 2013.

40 Habarulema, J. B. and Carelse, S. A.: Long-term analysis between radio occultation and ionosonde
41 peak electron density and height during geomagnetic storms. *Geophysical Research Letters*,
42 43(9), 4106-4111, 2016.

43 Habarulema, J. B., Katamzi, Z. T., and Yizengaw, E.: First observations of poleward large-scale
44 traveling ionospheric disturbances over the African sector during geomagnetic storm

1 conditions. *Journal of Geophysical Research: Space Physics*, 120(8), 6914-6929, 2015.

2 Habarulema, J. B., Katamzi, Z. T., Yizengaw, E., Yamazaki, Y., and Seemala, G.: Simultaneous
3 storm time equatorward and poleward large-scale TIDs on a global scale. *Geophysical*
4 *Research Letters*, 43(13), 6678-6686, 2016.

5 Habarulema, J. B., Yizengaw, E., Katamzi-Joseph, Z. T., Moldwin, M. B., and Buchert, S.: Storm
6 Time Global Observations of Large - Scale TIDs From Ground - Based and In Situ Satellite
7 Measurements. *Journal of Geophysical Research: Space Physics*, 123(1), 711-724, 2018.

8 Hines, C. O.: Internal atmospheric gravity waves at ionospheric heights. *Canadian Journal of*
9 *Physics*, 38(11), 1441-1481, 1960.

10 Ho, C. M., Mannucci, A. J., Lindqwister, U. J., Pi, X., and Tsurutani, B. T.: Global ionosphere
11 perturbations monitored by the worldwide GPS network. *Geophysical Research*
12 *Letters*, 23(22), 3219-3222, 1996.

13 Hocke, K. and Schlegel, K.: A review of atmospheric gravity waves and travelling ionospheric
14 disturbances: 1982-1995. In *Annales Geophysicae* (Vol. 14, No. 9, p. 917), 1996.

15 Hunsucker, R. D.: Atmospheric gravity waves generated in the high-latitude ionosphere: A
16 review. *Reviews of Geophysics*, 20(2), 293-315, 1982.

17 Jonah, O. F., Coster, A., Zhang, S., Goncharenko, L., Erickson, P. J., Paula, E. R., and Kherani, E.
18 A.: TID observations and source analysis during the 2017 Memorial Day weekend
19 geomagnetic storm over North America. *Journal of Geophysical Research: Space Physics*,
20 123, 8749– 8765. <https://doi.org/10.1029/2018JA025367>, 2018.

21 Klausner, V., Fagundes, P. R., Sahai, Y., Wrasse, C. M., Pillat, V. G., and Becker-Guedes, F.:
22 Observations of GW/TID oscillations in the F2 layer at low latitude during high and low
23 solar activity, geomagnetic quiet and disturbed periods. *Journal of Geophysical Research:*
24 *Space Physics*, 114(A2), 2009.

25 Klobuchar, J. A.: Design and characteristics of the GPS ionospheric time delay algorithm for
26 single frequency users. In *PLANS'86-Position Location and Navigation Symposium* (pp.
27 280-286), 1986.

28 Krankowski, A., Zakharenkova, I., Krypiak-Gregorczyk, A., Shagimuratov, I. I., and Wielgosz, P.:
29 Ionospheric electron density observed by FORMOSAT-3/COSMIC over the European region
30 and validated by ionosonde data. *Journal of Geodesy*, 85(12), 949-964, 2011.

31 Lanyi, G. E. and Roth, T.: A comparison of mapped and measured total ionospheric electron
32 content using global positioning system and beacon satellite observations. *Radio*
33 *Science*, 23(4), 483-492, 1988.

34 Lyons, L. R., Nishimura, Y., Zhang, S. R., Coster, A. J., Bhatt, A., Kendall, E., and Deng, Y.:
35 Identification of Auroral Zone Activity Driving Large-Scale Traveling Ionospheric
36 Disturbances. *Journal of Geophysical Research: Space Physics*, 124(1), 700-714, 2019.

37 Maeda, S. and Handa, S.: Transmission of large-scale TIDs in the ionospheric F2-region. *Journal*
38 *of Atmospheric and Terrestrial Physics*, 42(9-10), 853-859, 1980.

39 Mendillo, M. and Narvaez, C.: Ionospheric storms at geophysically-equivalent sites–Part 1:
40 Storm-time patterns for sub-auroral ionospheres. In *Annales Geophysicae* (Vol. 27, No. 4, pp.
41 1679-1694). Copernicus GmbH, 2009.

42 Morton, F. W. and Essex, E. A.: Gravity wave observations at a southern hemisphere mid-latitude
43 station using the total electron content technique. *Journal of Atmospheric and Terrestrial*
44 *Physics*, 40(10-11), 1113-1122, 1978.

- 1 Nicolls, M. J., Kelley, M. C., Coster, A. J., González, S. A., and Makela, J. J.: Imaging the
2 structure of a large-scale TID using ISR and TEC data. *Geophysical Research Letters*, 31(9),
3 2004.
- 4 Pederick, L. H., Cervera, M. A., and Harris, T. J.: Interpreting observations of large-scale traveling
5 ionospheric disturbances by ionospheric sounders. *Journal of Geophysical Research: Space*
6 *Physics*, 122(12), 2017.
- 7 Pradipta, R., Valladares, C. E., Carter, B. A., and Doherty, P. H.: Interhemispheric propagation and
8 interactions of auroral traveling ionospheric disturbances near the equator. *Journal of*
9 *Geophysical Research: Space Physics*, 121(3), 2462-2474, 2016.
- 10 Ramsingh, Sripathi, S., Sreekumar, S., Banola, S., Emperumal, K., Tiwari, P., and Kumar, B. S.:
11 Low - latitude ionosphere response to super geomagnetic storm of 17/18 March 2015:
12 Results from a chain of ground - based observations over Indian sector. *Journal of*
13 *Geophysical Research: Space Physics*, 120(12), 10-864, 2015.
- 14 Richmond, A. D. and Roble, R. G.: Dynamic effects of aurora-generated gravity waves on the
15 mid-latitude ionosphere. *Journal of Atmospheric and Terrestrial Physics*, 41(7-8), 841-852,
16 1979.
- 17 Rideout, W. and Coster, A.: Automated GPS processing for global total electron content data. *GPS*
18 *Solutions*, 10(3), 219-228, 2006.
- 19 Saito, A., Fukao, S., and Miyazaki, S.: High resolution mapping of TEC perturbations with the
20 GSI GPS network over Japan. *Geophysical research letters*, 25(16), 3079-3082, 1998.
- 21 Saito, A., Nishimura, M., Yamamoto, M., Fukao, S., Kubota, M., Shiokawa, K., Otsuka, Y.,
22 Tsugawa, T., Ogawa, T., Ishii, M., Sakanoi, and T., Miyazaki, S.: Traveling ionospheric
23 disturbances detected in the FRONT campaign. *Geophysical Research Letters*, 28(4),
24 689-692, 2001.
- 25 Shiokawa, K., Otsuka, Y., Ogawa, T., Balan, N., Igarashi, K., Ridley, A. J., Knipp, D. J., Saito, A.,
26 and Yumoto, K.: A large-scale traveling ionospheric disturbance during the magnetic storm of
27 15 September 1999. *Journal of Geophysical Research: Space Physics*, 107(A6), SIA-5, 2002.
- 28 Song, Q., Ding, F., Wan, W., Ning, B., Liu, L., Zhao, B., Li, Q., and Zhang, R.: Statistical study of
29 large-scale traveling ionospheric disturbances generated by the solar terminator over
30 China. *Journal of Geophysical Research: Space Physics*, 118(7), 4583-4593, 2013.
- 31 Thomas, E. G., Baker, J. B. H., Ruohoniemi, J. M., Coster, A. J., and Zhang, S. R.: The
32 geomagnetic storm time response of GPS total electron content in the North American
33 sector. *Journal of Geophysical Research: Space Physics*, 121(2), 1744-1759, 2016.
- 34 Tsugawa, T., Saito, A., Otsuka, Y., and Yamamoto, M.: Damping of large-scale traveling
35 ionospheric disturbances detected with GPS networks during the geomagnetic storm. *Journal*
36 *of Geophysical Research: Space Physics*, 108(A3), 2003.
- 37 Tsugawa, T., Saito, A., and Otsuka, Y.: A statistical study of large-scale traveling ionospheric
38 disturbances using the GPS network in Japan. *Journal of Geophysical Research: Space*
39 *Physics*, 109(A6), 2004.
- 40 Tsugawa, T., Shiokawa, K., Otsuka, Y., Ogawa, T., Saito, A., and Nishioka, M.: Geomagnetic
41 conjugate observations of large-scale traveling ionospheric disturbances using GPS networks
42 in Japan and Australia. *Journal of Geophysical Research: Space Physics*, 111(A2), 2006.
- 43 Wan, W., Ning, B., Yuan, H., Li, J., Li, L., and Liang, J.: TID observation using a short baseline
44 network of GPS receivers. *Acta Geodaetica et Geophysica Hungarica*, 32(3-4), 321-327,

1 1997.

2 Wang, C.: New Chains of Space Weather Monitoring Stations in China, *Space*
3 *Weather*, 8, S08001, doi:10.1029/2010SW000603, 2010.

4 Zakharenkova, I., Astafyeva, E., and Cherniak, I.: GPS and GLONASS observations of large-scale
5 traveling ionospheric disturbances during the 2015 St. Patrick's Day storm. *Journal of*
6 *Geophysical Research: Space Physics*, 121(12), 2016.

7 Zhang, D. H. and Xiao, Z.: Study of ionospheric response to the 4B flare on 28 October 2003
8 using International GPS Service network data. *Journal of Geophysical Research: Space*
9 *Physics*, 110(A3), 2005.

10 Zhang, D. H., Zhang, W., Li, Q., Shi, L. Q., Hao, Y. Q., and Xiao, Z.: Accuracy analysis of the
11 GPS instrumental bias estimated from observations in middle and low latitudes. In *Annales*
12 *Geophysicae* (Vol. 28, No. 8, pp. 1571-1580). Copernicus GmbH, 2010.

13 Zhang, S. R., Foster, J. C., Coster, A. J., and Erickson, P. J.: East-West Coast differences in total
14 electron content over the continental US. *Geophysical Research Letters*, 38(19), 2011.

15 Zhang, S. R., Erickson, P. J., Goncharenko, L. P., Coster, A. J., Rideout, W., and Vierinen, J.:
16 Ionospheric bow waves and perturbations induced by the 21 August 2017 solar
17 eclipse. *Geophysical Research Letters*, 44(24), 12-067, 2017.

18 Zhang, W., Zhang, D. H., and Xiao, Z.: The influence of geo-magnetic storms on the estimation of
19 GPS instrumental biases, *Ann. Geophys.*, 27, 1613-1623, doi:10.5194/angeo-27-1613-2009,
20 2009.

21

1 **Captions of Table and Figures**

2 **Table 1.** The estimated propagation parameters of the LSTID and the corresponding standard
3 errors. The second column contains the propagation directions, which are measured clockwise
4 from the South. V_t/V_c represents the phase speed estimated with certain wave trough/crest.

5

6 **Figure 1.** Locations of the GPS stations of different networks (colored dots), the HF Doppler shift
7 stations (green stars), the National Time Service Center of China (grey stars), and the ionosondes
8 (green triangles) that used in this study.

9

10 **Figure 2.** Temporal variations of (a) the solar wind speed (V_{sw}), (b) the IMF Bz component, (c)
11 the SYM-H index, and (d) the AE index between 18:00 UT, 16 March 2015 and 06:00 UT, 18
12 March 2015. The occurrence of SSC is shown with vertical dashed lines.

13

14 **Figure 3.** Temporal variations of the HF Doppler shift records from (a) MDT and (b) SZT
15 between 08:00 UT and 14:00 UT, 17 March 2015.

16

17 **Figure 4.** A series of 2D VTECP' maps over the East Asian sector from the period of 09:40-09:50
18 UT to 11:30-11:40 UT on 17 March 2015. The grey areas represent the nightside. The colorbar
19 represents the VTECP' (units: TECu). The green and yellow lines illustrate the least square
20 fittings (order 2) for wavefronts.

21

22 **Figure 5.** Temporal variations of mean VTECP' near the Doppler reflection points between 08:00
23 UT and 14:00 UT, 17 March 2015.

24

25 **Figure 6.** Temporal variations of the virtual height for iso-frequency lines from 8 ionosondes
26 between 08:00 UT and 12:00 UT, 17 March 2015. Frequencies are depicted on each iso-frequency
27 line. The time resolution is 15 min for all stations. The red dashed lines connect the peaks of the
28 highest and lowest frequencies.

29

30 **Figure 7.** A detailed example of the wavefront fitting method. Green dots indicate the data points
31 for least square fitting. Green arrows depict the propagation orientations in different longitudes.
32 Dashed black rectangles mark the areas for generating TLPs in Figure 8.

33

34 **Figure 8.** TLPs of VTECP' for different longitudinal bands between 07:00-14:00 UT. White dots
35 give the data points for linear fitting, and the fitting results are marked with white lines. Black
36 dashed lines depict 30°N in (b-d, f) and 40°N in (f).

37

38 **Figure 9.** The sketch of (upper) the geomagnetic declination angles and (lower) the propagation
39 directions in different longitudes on the wavefront fitted in Figure 7. The propagation directions
40 are measured clockwise from the South.

41

42 **Figure 10.** The TLP of VTECP' for the European sector (10°E-20°E, 30°N-70°N) between
43 01:00-23:00 UT. White lines and dots are similar to those in Figure 8. The black dashed line
44 depicts 60°N.

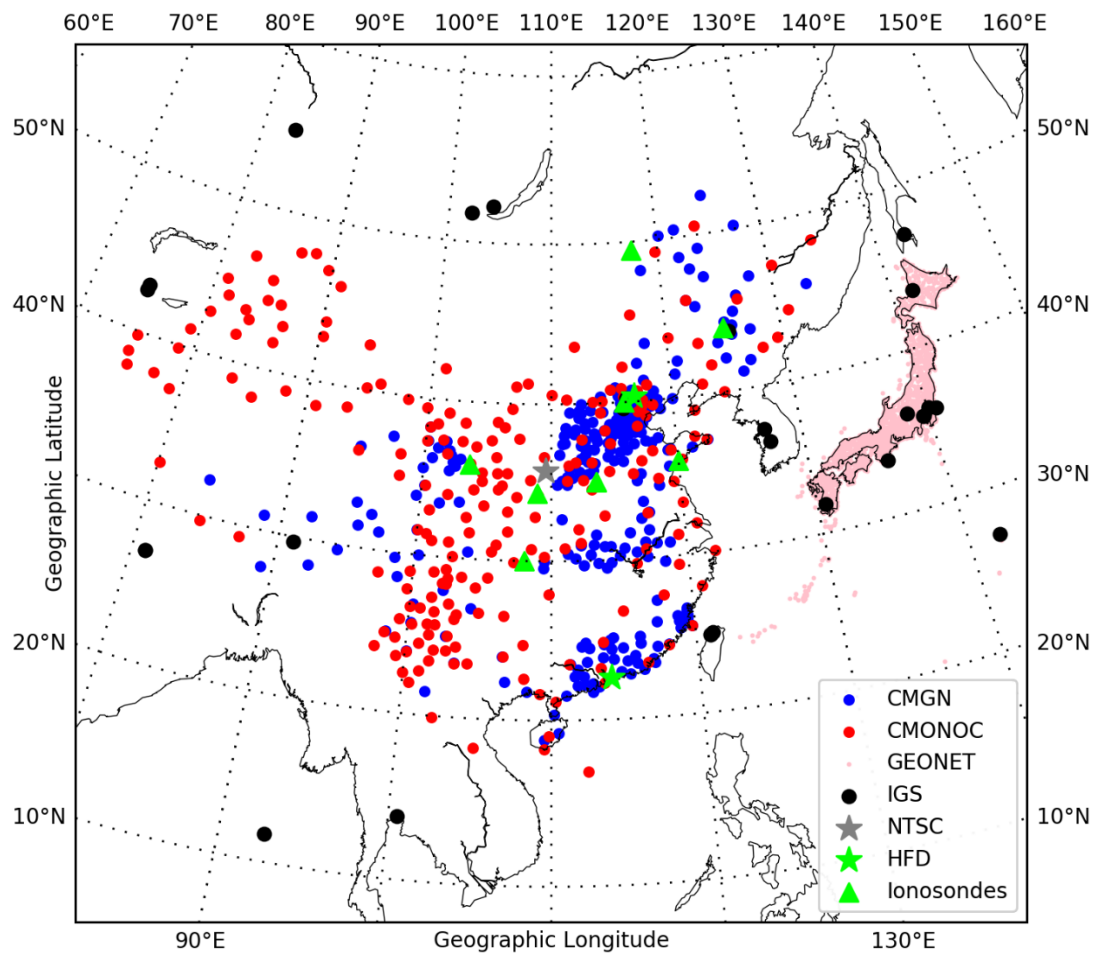
1 **Table 1.**

Lon. (°E)	Dir. (°)	Period (min)	Vt (m/s)	Vc (m/s)	Wavelength (km)
80-90	-11.2	81.1 ± 3.4	500 ± 40	542 ± 31	2536 ± 163
90-100	-7.1	77.6 ± 5.2	552 ± 22	670 ± 44	2845 ± 222
100-110	-2.9	58.8 ± 1.5	587 ± 47	638 ± 76	2160 ± 167
110-120	1.3	62.4 ± 2.0	605 ± 27	562 ± 25	2184 ± 99
120-130	7.9	94.2 ± 1.3	647 ± 39	673 ± 63	3731 ± 216

2

3

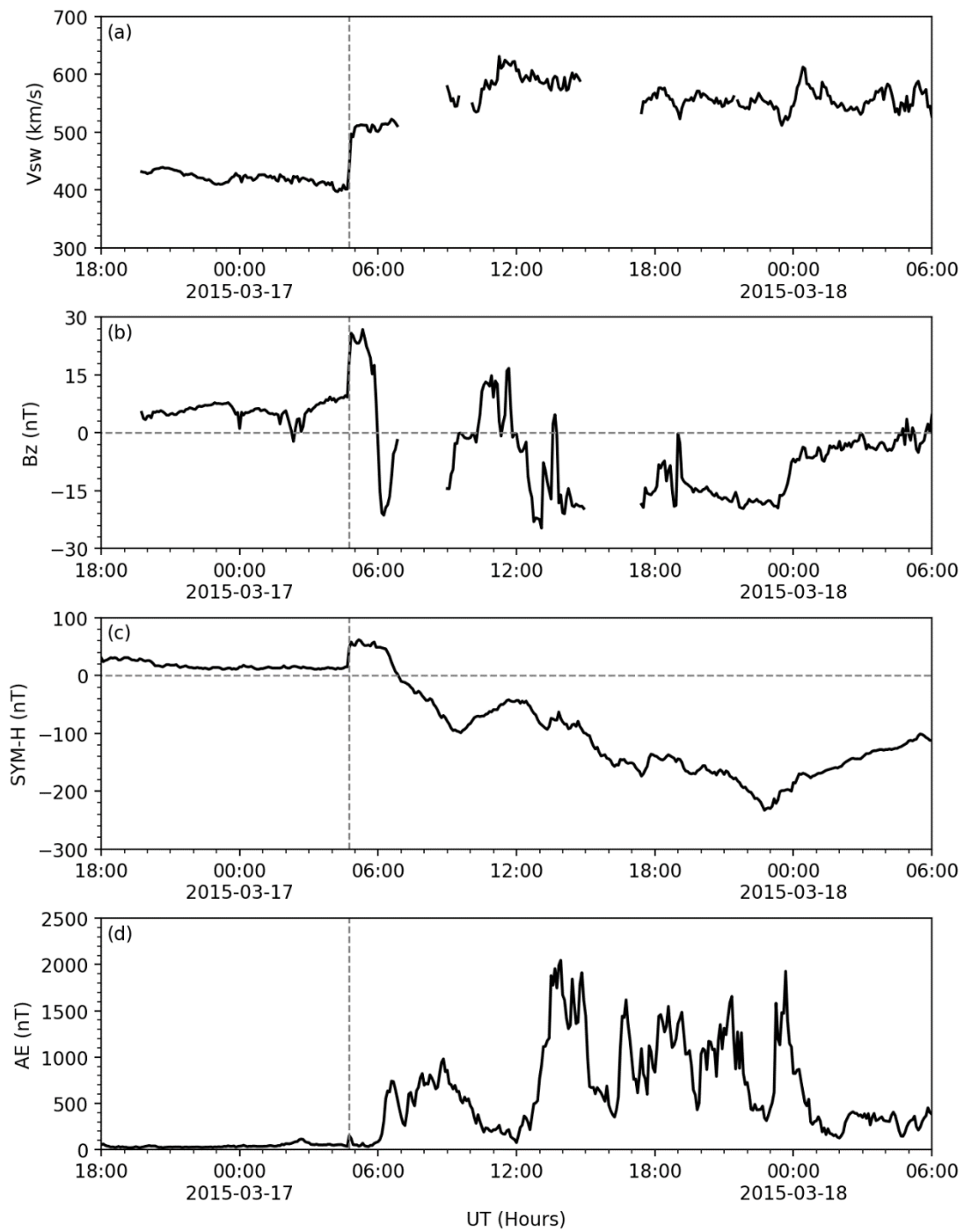
1 Figure 1.



2

3

1 Figure 2.

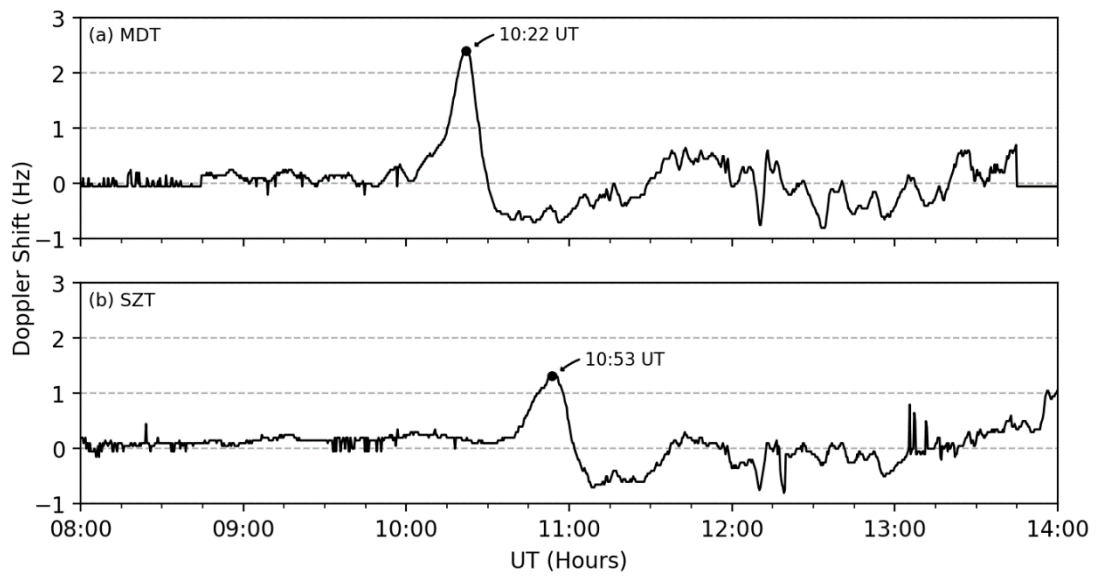


2

3

4

1 Figure 3.



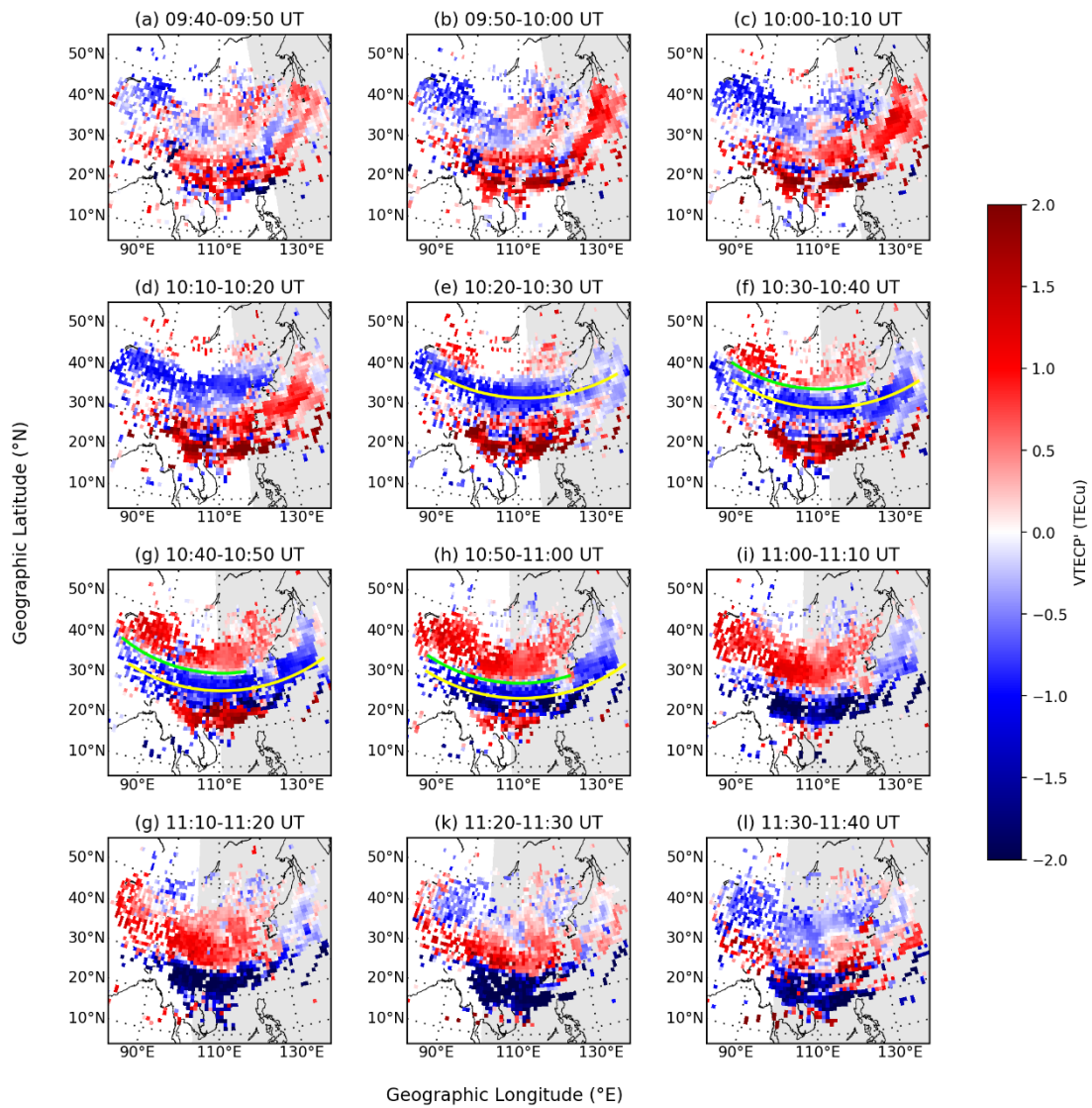
2

3

4

5

1 Figure 4.

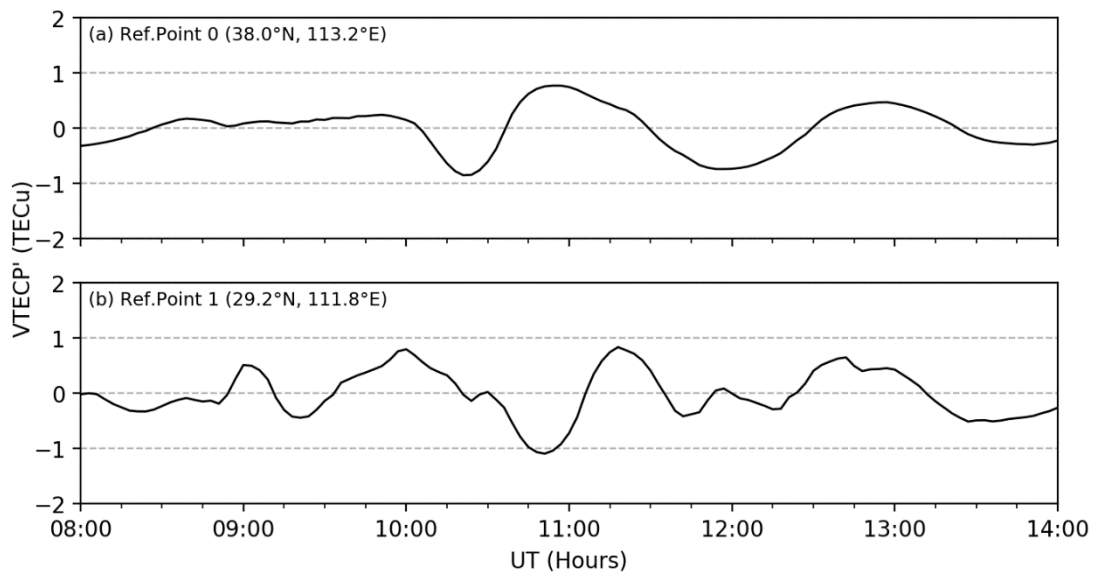


2

3

4

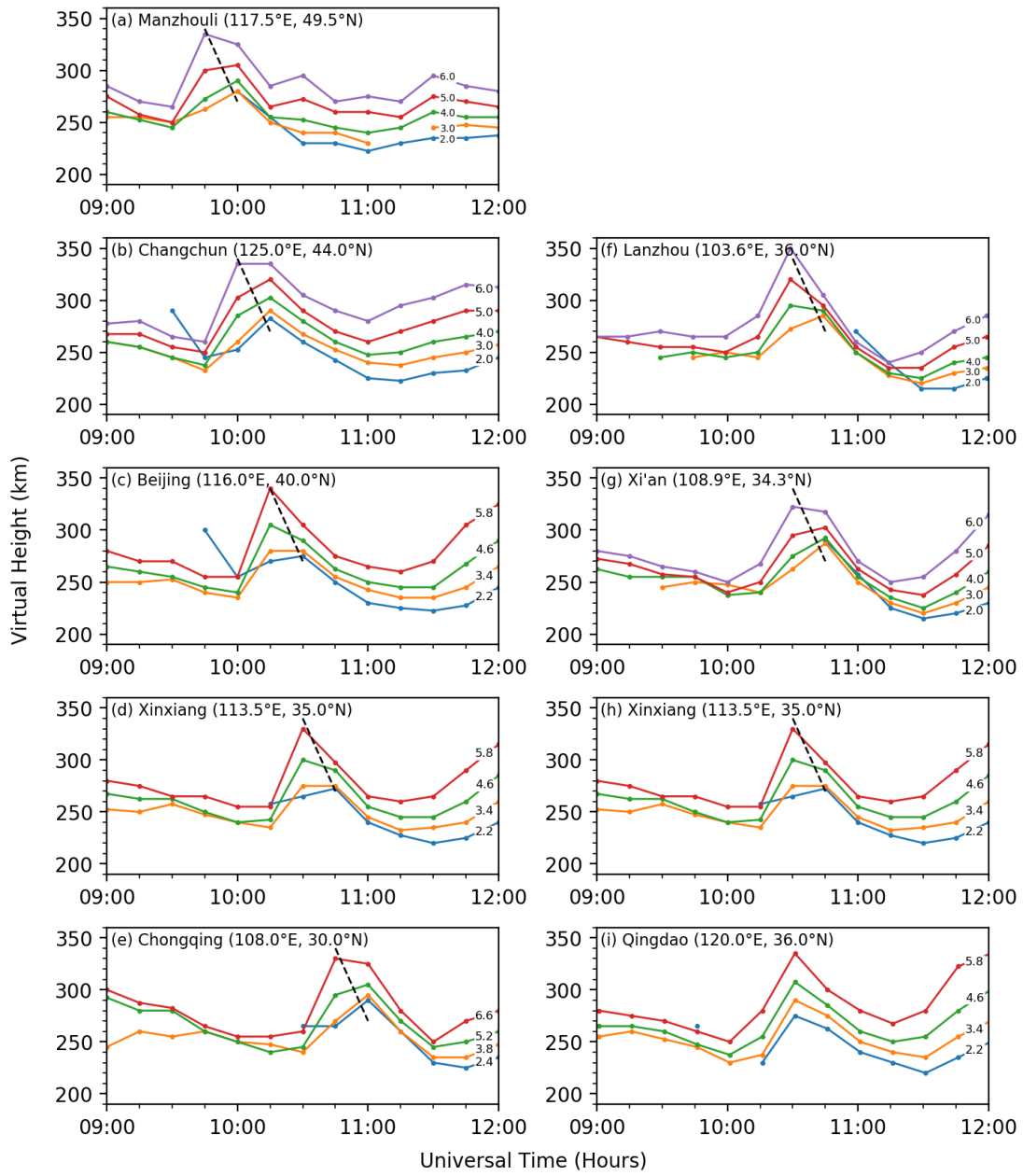
1 Figure 5.



2

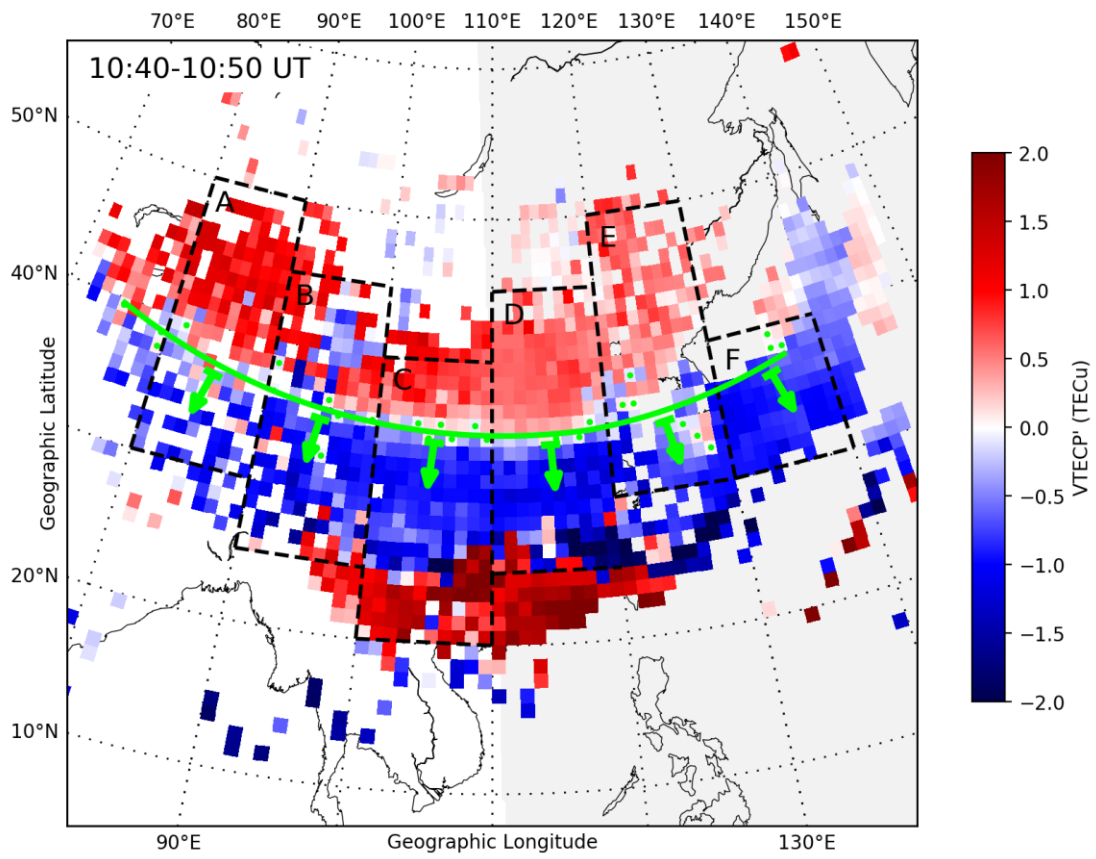
3

1 Figure 6.



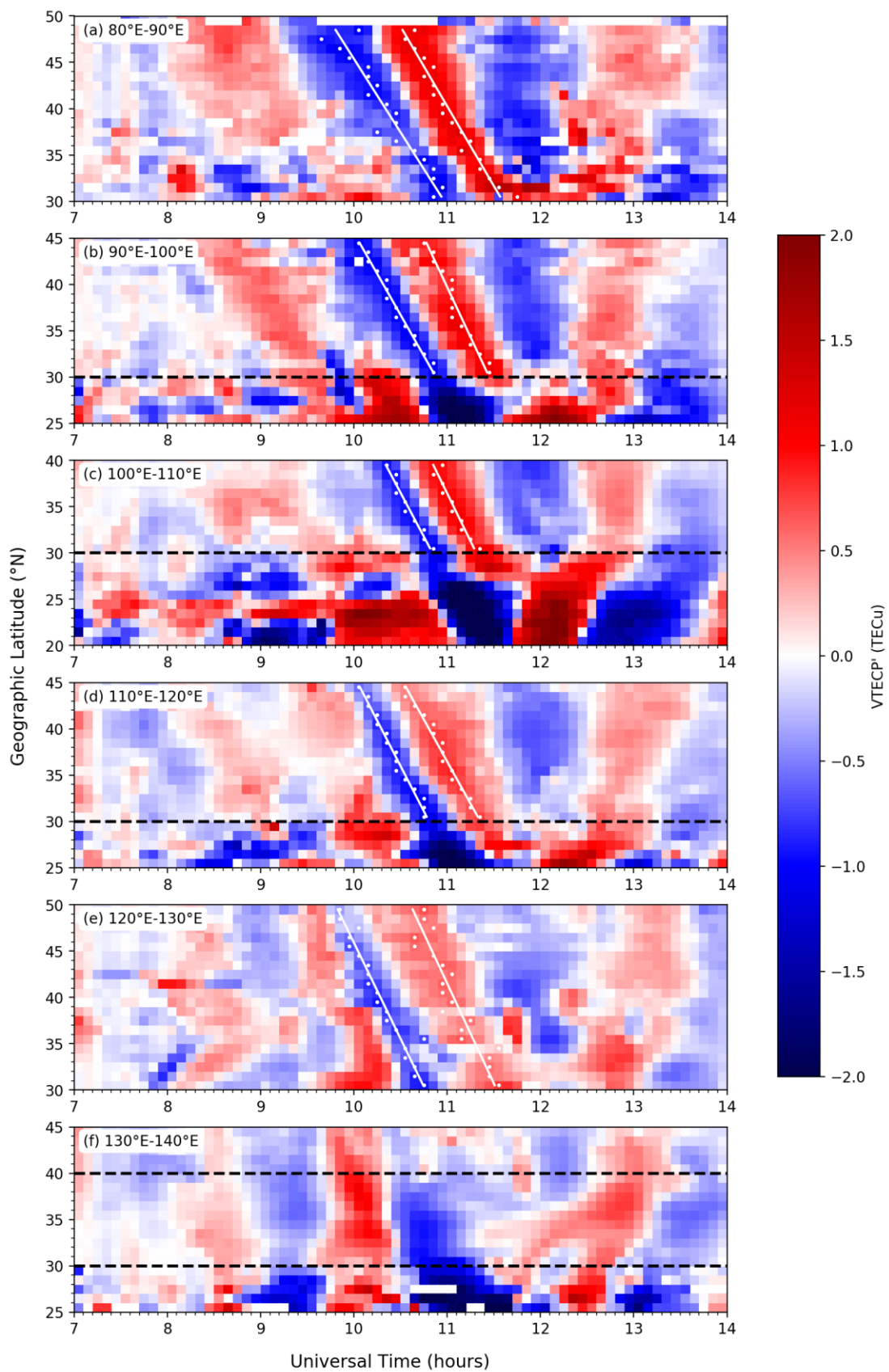
2
3
4

1 Figure 7.



2
3
4
5

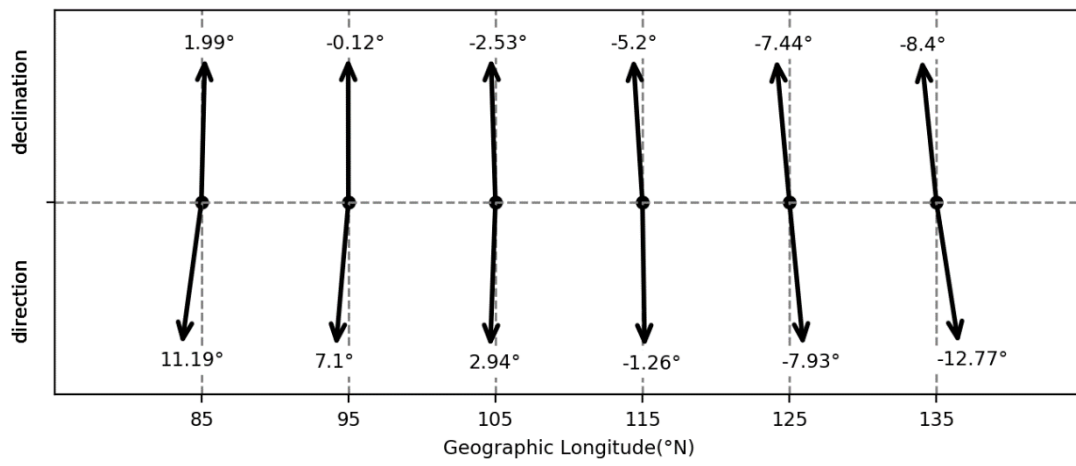
1 Figure 8.



2

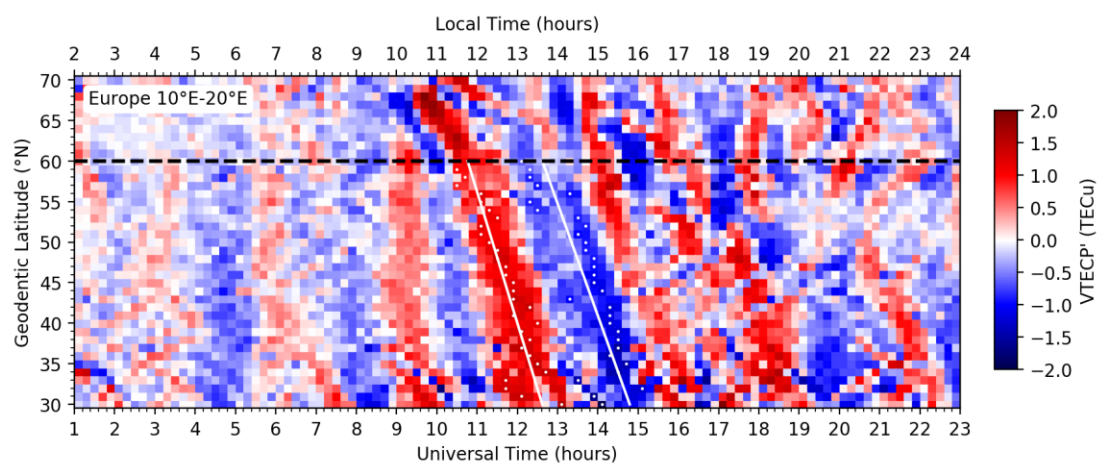
3

1 Figure 9.



2
3
4

1 Figure 10.



2

3